JACS
JOURNAL OF THE AMERICAN CHEMICAL SOCIETY
Article
pubs.acs.org/JACS

Charge Transfer Stabilization of Late Transition Metal Oxide Nanoparticles on a Layered Niobate Support

Megan E. Strayer,[†] Thomas P. Senftle,[‡] Jonathan P. Winterstein,[§] Nella M. Vargas-Barbosa,[†] Renu Sharma,[§] Robert M. Rioux,[†,‡] Michael J. Janik,*[,‡] and Thomas E. Mallouk*[,†]

[†]Departments of Chemistry, Physics, and Biochemistry and Molecular Biology and [‡]Department of Chemical Engineering, The Pennsylvania State University, University Park, Pennsylvania 16802, United States

[§]Center for Nanoscale Science and Technology, National Institute of Standards and Technology, Gaithersburg, Maryland 20899, United States

Supporting Information

ABSTRACT: Interfacial interactions between late transition metal/metal oxide nanoparticles and oxide supports impact catalytic activity and stability. Here, we report the use of isothermal titration calorimetry (ITC), electron microscopy and density functional theory (DFT) to explore periodic trends in the heats of nanoparticle−support interactions for late transition metal and metal oxide nanoparticles on layered niobate and silicate supports. Data for $Co(OH)_2$, hydroxyiridate-capped $IrO_x{\cdot}nH_2O$, $Ni(OH)_2$, CuO, and Ag_2O nanoparticles were added to previously reported data for $Rh(OH)_3$ grown on nanosheets of $TBA_{0.24}H_{0.76}Ca_2Nb_3O_{10}$ and a layered silicate. ITC measurements showed stronger bonding energies in the order Ag < Cu ≈ Ni ≈ Co < Rh < Ir on the niobate support, as expected from trends in M−O bond energies. Nanoparticles with exothermic heats of interaction were stabilized against sintering. In contrast, ITC measurements showed endothermic interactions of Cu, Ni, and Rh oxide/hydroxide nanoparticles with the silicate and poor resistance to sintering. These trends in interfacial energies were corroborated by DFT calculations using single-atom and four-atom cluster models of metal/metal oxide nanoparticles. Density of states and charge density difference calculations reveal that strongly bonded metals (Rh, Ir) transfer d-electron density from the adsorbed cluster to niobium atoms in the support; this mixing is absent in weakly binding metals, such as Ag and Au, and in all metals on the layered silicate support. The large differences between the behavior of nanoparticles on niobate and silicate supports highlight the importance of d-orbital interactions between the nanoparticle and support in controlling the nanoparticles' stability.

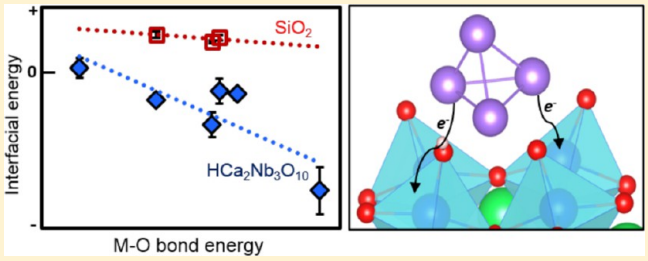

INTRODUCTION

Late transition metal nanoparticles dispersed on high surface area oxide supports are essential to technologies in the energy, chemical, and environmental industries, where they are employed as catalysts and electrocatalysts. The activity and selectivity of these catalysts are dependent on the size[1−8] and shape[9] of the active nanoparticles, the composition of the oxide support,[1−5,10] and the extent of support reduction.[4,5,11−15] Therefore, the interfacial interactions between catalytic nanoparticles and supports are key parameters in determining catalyst stability, activity and selectivity.

Under catalytic reaction conditions, nanoparticles can grow to form larger, less active particles. The rate and extent of particle growth is controlled in large measure by the details of the nanoparticle/support interface. Both theoretical[16−20] and experimental studies[4,21−25] have investigated the atomic-level structure of this interface. Although nanoparticle−support interactions are clearly implicated in the migration of particles leading to coalescence and in the kinetics of Ostwald ripening, there is still relatively little direct experimental quantification of the bonding at the nanoparticle−support interface.[4,26]

To understand these interactions, Campbell and co-workers have recently measured the enthalpy of interfacial bonding using a piezoelectric metal adsorption calorimeter.[27] Atoms of elemental Ag, Cu, Ca, Li, and Pb were vapor deposited onto single crystal oxide supports, including MgO, CeO_2 and Fe_3O_4. The heat of interaction was found to be strongly dependent on both the nanoparticle size and support composition (ref 4 and references within).

More recently, we reported the use of solution-based isothermal titration calorimetry (ITC) to quantify the heat of interaction between rhodium hydroxide nanoparticles and several early transition metal oxide and main group oxide supports.[26] These heats were also found to be strongly dependent on the oxide support composition. Stronger interfacial bonding was found to inhibit nanoparticle sintering in vacuum and under reducing atmospheres at elevated temperatures. Rhodium hydroxide nanoparticles bond exothermically to early transition metal (niobium, tantalum, and

Received: October 27, 2015
Published: December 10, 2015

ACS Publications © 2015 American Chemical Society

DOI: 10.1021/jacs.5b11230
J. Am. Chem. Soc. 2015, 137, 16216−16224

tungsten) oxide supports, which inhibit nanoparticle sintering. Conversely, the interfacial bonding to main group oxide supports, such as silica and alumina, is endothermic and particle growth on these oxides occurs at a much lower temperature.[26]

In the present study, we combine calorimetric measurements with density functional theory (DFT) calculations to map out the periodic trends in the strength of the nanoparticle−support interaction and to understand the reason for the anomalously strong bonding of late transition metals to early transition metal oxides. ITC was used to quantify the heats of interaction of cobalt, iridium, nickel, copper and silver metal oxide/hydroxide nanoparticles to a layered niobium oxide support and compared to a high surface area silicon oxide support. In situ high-resolution transmission electron microscopy (HRTEM) and high-angle annular dark field scanning transmission electron microscopy (HAADF STEM) were used to track the sintering of nanoparticles as a function of temperature under vacuum. A clear correlation between the strength of interfacial bonding and the resistance of nanoparticles to growth in vacuum was observed. DFT calculations of model systems were consistent with the experimental data and provided insight into the nature of charge transfer interactions that strongly stabilize late transition metal/metal oxide nanoparticles on early transition metal oxide supports.

MATERIALS AND METHODS

Supported Nanoparticle Synthesis. The layered oxide $KCa_2Nb_3O_{10}$ was synthesized as previously reported.[28] Briefly, a 0.4 mol/mol (mole fraction) stoichiometric excess of K_2CO_3 was ground with stoichiometric amounts of $CaCO_3$ and Nb_2O_5. The powder mixture was heated at 1200 °C for 12 h in an alumina crucible. The obtained powder (1.00 g) was mixed with 1.0 mol L^{-1} HCl (100 mL), and the solution was changed daily for 3 days to produce the proton-exchanged product $HCa_2Nb_3O_{10}\cdot 0.5H_2O$.[29] Nanosheets of $TBA_{0.24}H_{0.76}Ca_2Nb_3O_{10}$ were obtained by mixing 0.12 g $HCa_2Nb_3O_{10}\cdot 0.5H_2O$ with 50 mL of 25.0 mmol L^{-1} tetra(*n*-butylammonium) hydroxide (TBA^+OH^-) solution and stirring overnight.[26] Na-TSM ($Na_{0.66}Mg_{2.68}(Si_{3.98}Al_{0.02})O_{10.02}F_{1.96}$) (1.00 g) was added to 100 mL of deionized water and stirred overnight to exfoliate into nanosheets. Concentrated NaOH was used to bring the Na-TSM solution to a pH of 12.0 before metal oxide/hydroxide nanoparticle deposition. Commercially purchased SiO_2 with an average particle diameter of (17 ± 6) nm (n = 101) and a surface area of (408 ± 8) m^2 g^{-1} was also brought to a pH of 12.0 before nanoparticle deposition.

Cobalt hydroxide, nickel hydroxide, copper oxide and silver oxide nanoparticles were deposited as previously reported for rhodium hydroxide nanoparticle deposition.[26,30,31] 20 mmol L^{-1} aqueous solutions were made from the metal salts $CoBr_2$, $NiSO_4\cdot 6H_2O$, $CuSO_4$, and $AgNO_3$. Appropriate amounts of the metal aqueous solutions were added to 50.0 mL exfoliated nanosheets to achieve a metal mass fraction deposition of 0.05. The reaction was stirred for 18 h at room temperature. The nanosheets were then restacked by dripping the suspension into 2 mol L^{-1} KOH (50 mL). The solid sample was washed twice more with KOH and three times with water before drying at 60 °C overnight.

An iridium colloidal solution containing both monomeric iridium ($[Ir(OH)_5(H_2O)]^{2-}$) and $IrO_x\cdot nH_2O$ nanoparticles was synthesized as previously reported.[32] In the modified preparation, 2.0 mmol K_2IrCl_6 was dissolved in 80 mmol L^{-1} NaOH (90.0 mL), heated rapidly until the temperature reached 75 °C, then immediately cooled in an ice bath for 64 h. During the 64 h of ice bath cooling, the pH was monitored closely and kept at 11.9 with the addition of 1.0 mol L^{-1} NaOH. After 64 h, the solution volume was adjusted to 100 mL with nanopure water. Purified $IrO_x\cdot nH_2O$ nanoparticles were obtained by precipitating the above product with double volume isopropyl alcohol (IPA) and resuspending the precipitate in deionized water.[32] A more dilute 0.5 mmol L^{-1} iridium monomer solution (which contains little or no colloidal $IrO_x\cdot nH_2O$) was synthesized by the addition of 0.025 mmol K_2IrCl_6 to 50.0 mL of 0.100 mmol L^{-1} TBA^+OH^-, heating the solution to 70 °C until the solution turned colorless, and then being cooled immediately in an ice bath.[32] The iridium species were deposited by adding 1.6 mL of the 20 mmol L^{-1} solution to 50.0 mL of the nanosheet solution to achieve a mass fraction of 0.05. The nanosheets were restacked as detailed above for the other nanoparticles.

For nanoparticles deposited onto Na-TSM, the composite was centrifuged without KOH restacking and washed three times with water before drying overnight at 60 °C.

Characterization. Isothermal titration calorimetry (ITC) experiments were performed using a 1.04 mL cell. Measurements were conducted as previously reported.[26] Aqueous metal halide precursors (10 mmol L^{-1} to 15 mmol L^{-1}) were injected from the syringe into solutions of $TBA_{0.24}H_{0.76}Ca_2Nb_3O_{10}$ nanosheets (0.1 mmol L^{-1} to 4 mmol L^{-1}). The iridium monomer solution was injected as a 0.5 mmol L^{-1} solution. A titration occurred every 25 min for the duration of the experiment (34 titrations). Experiments were done at 25 °C and in triplicate. The data was fit using an independent bonding model, and heats of dilution were subtracted from each run to retrieve thermochemical data.

High-resolution transmission electron microscopy (HRTEM) and high-angle annular dark field (HAADF) scanning transmission electron microscopy (STEM) images were obtained on a TEM with an accelerating voltage of 300 kV. For temperature-dependent TEM experiments, samples were dispersed in an IPA solution, drop cast on a temperature-controlled support and then dried under a heat lamp. Ambient temperature TEM images were retrieved after drop-casting sample from solution onto a lacey carbon TEM grid.

A powder X-ray diffractometer with monochromatized Cu Kα radiation and a wavelength of 0.15418 nm was used to obtain powder X-ray diffraction (XRD) patterns.

For all measured values, the uncertainty is given as one standard deviation of the mean. The number of measurements for a measured value (n) is given throughout the text.

Electronic Structure Calculations. DFT calculations were conducted utilizing the Vienna ab initio simulation package (VASP).[33,34] The exchange-correlation energy functional was treated using the generalized gradient approximation (GGA) implemented in the Perdew−Wang formulation (PW91).[35] Plane-wave basis sets were employed for all periodic calculations with an energy cutoff of 450 eV (4.34×10^4 kJ mol^{-1}). The projector augmented wave pseudo potential approximation[36] (PAW) was used to represent core electronic regions, with the following electronic valence configurations: $4p^64d^45s^1$ for Nb, $3p^23d^64s^2$ for Ca, $3s^23p^2$ for Si, $2s^22p^4$ for O, $1s^1$ for H, $3d^74s^2$ for Co, $4p^64d^85s^1$ for Rh, $5d^76s^2$ for Ir, $3d^84s^2$ for Ni, $4d^{10}$ for Pd, $5d^96s^1$ for Pt, $3d^{10}4s^1$ for Cu, $4d^{10}5s^1$ for Ag, and $5d^{10}6s^1$ for Au. All calculations were spin polarized, and when necessary, multiple spin states were tested to ensure that the optimal spin state was identified. Monkhorst−Pack[37] (MP) Brillouin zone sampling was employed with a 4 × 4 × 1 MP k-point spacing for calculations on the $HCa_2Nb_3O_{10}$ surface model (this was reduced to 3 × 3 × 1 MP for the 2 × 2 supercell model used for calculations involving larger M_4 clusters), and a 2 × 2 × 1 MP k-point sampling for the SiO_2 surface model. Single metal atom calculations were completed in a 4.5 nm × 4.5 nm × 4.5 nm periodic box at the Γ point. Conjugant gradient structural relaxations were employed with an atomic force convergence criterion of 0.05 eV $Å^{-1}$ (48.2 kJ mol^{-1} nm^{-1}). Partial charges on atoms were computed using the Bader method.[38,39]

RESULTS AND DISCUSSION

Nanoparticle Deposition on Layered Oxide Supports. Nanosheets derived from the layer perovskite $KCa_2Nb_3O_{10}$, and the synthetic mica Na-TSM were used as model early transition metal oxide and main group oxide supports, respectively. As in

DOI: 10.1021/jacs.5b11230
J. Am. Chem. Soc. 2015, 137, 16216−16224

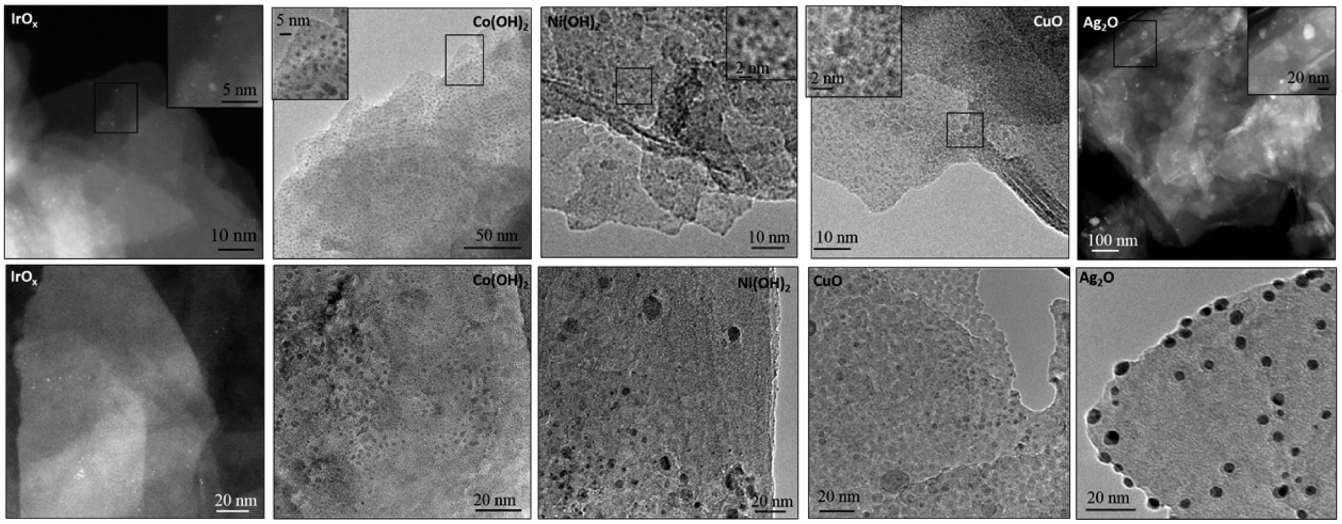

Figure 1. Ambient temperature HRTEM and HAADF STEM images of nanoparticles deposited at room temperature on $KCa_2Nb_3O_{10}$ (top) and Na-TSM (bottom).

our earlier study,[26] the use of these nanosheets enabled observation of nanoparticle growth on the crystallographically well-defined basal plane surface, and provided thin, electron-transparent samples for imaging of the nanoparticles by HRTEM and HAADF STEM. The phase purity of $KCa_2Nb_3O_{10}$ and its acid-exchanged derivative $HCa_2Nb_3O_{10}\cdot 0.5H_2O$ were confirmed by comparing XRD patterns to literature reports.[28] $HCa_2Nb_3O_{10}\cdot 0.5H_2O$ was exfoliated into nanosheets of $TBA_{0.24}H_{0.76}Ca_2Nb_3O_{10}$ in excess aqueous TBA^+OH^- solutions as described previously.[26,29]

Our earlier study quantified the heat of interfacial bonding between Rh^{3+} hydroxide nanoparticles and oxide supports. To more broadly investigate periodic trends, the oxides/hydroxides of five additional late transition metal ions (Ir^{3+}, Co^{2+}, Ni^{2+}, Cu^{2+}, Ag^+) were investigated. These ions were selected based on the solubility of their halide salts and, in all cases except Ir^{3+}, the rapid ligand exchange kinetics of the metal aquo ions. Metal oxide/hydroxide nanoparticles were deposited onto $TBA_{0.24}H_{0.76}Ca_2Nb_3O_{10}$ and Na-TSM nanosheets by in situ alkaline hydrolysis of the metal salt precursor, at a mass fraction of 0.05 metal. The same metal salts were used in ITC experiments to measure the interfacial bonding heats, as described below. Table S1 lists the metal precursors used in this study, as well as the corresponding metal oxide/hydroxide nanoparticles formed. The phase of the deposited nanoparticle was determined by hydrolyzing the precursor salts in TBA^+OH^- in the absence of nanosheets, collecting the precipitate and identifying the solid by XRD (Figure S1).

The lattice constants of the nanoparticles made by hydrolysis in the absence of nanosheets are reported in Table S1. The XRD line widths indicate that $Co(OH)_2$ and CuO scattering domains are small, with estimated sizes of 5 and 13 nm, respectively. The line widths predict the Ag_2O scattering domains to be larger, with an estimated size of 30 nm. The $Ni(OH)_2$ XRD pattern contains both narrow and broad reflections, consistent with the platy texture of this layered compound, with estimated scattering domain sizes of 12 nm and 2 nm, respectively.

Since Ir^{3+} complexes have slow ligand exchange rates, direct alkaline hydrolysis of Ir(III) halides was impractically slow for ITC experiments. In this case, preformed aquo ions and colloidal particles were made by alkaline hydrolysis and then deposited onto the nanosheets. We have recently shown that the dissolution of dilute Ir(III) and Ir(IV) salts in alkaline solutions (pH > 13, [Ir] < 10^{-4} mmol L^{-1}) produces monomeric anions ($[Ir(OH)_5(H_2O)]^{2-}$ and $[Ir(OH)_6]^{2-}$), and that condensation of these ions at higher concentrations yields amorphous $IrO_x\cdot nH_2O$ nanoparticles, onto which the monomeric anions strongly adsorb.[32,40] This colloidal solution, with an average nanoparticle diameter of (1.2 ± 0.3) nm (n = 299), is shown in the TEM image in Figure S2.

This colloidal solution will be referred to as hydroxyiridate-capped $IrO_x\cdot nH_2O$ throughout this paper.

As we reported previously for $Rh(OH)_3$ nanoparticle deposition on $KCa_2Nb_3O_{10}$, turbostratic restacking of the nanosheets occurs upon addition of KOH to the suspensions. The XRD patterns of the restacked materials show only 00l and hk0 reflections of the nanosheets, and no reflections can be attributed to the nanoparticles.[30] All the late transition metal oxide/hydroxides deposited onto $KCa_2Nb_3O_{10}$ display these characteristic XRD patterns after restacking with KOH (Figure S3).

The HRTEM and HAADF STEM images on the top row of Figure 1 illustrate the size distribution of hydroxyiridate-capped $IrO_x\cdot nH_2O$, $Co(OH)_2$, $Ni(OH)_2$, CuO, and Ag_2O nanoparticles deposited onto $TBA_{0.24}H_{0.76}Ca_2Nb_3O_{10}$ nanosheets at ambient temperature, and Table 1 lists the deposited nanoparticle average diameter. Except in the case of Ag_2O,

Table 1. Average Nanoparticle Diameter of Metal Oxide/Hydroxide Nanoparticles Deposited onto Nanosheets of $TBA_{0.24}H_{0.76}Ca_2Nb_3O_{10}$ and Na-TSM at Room Temperature as Determined from TEM Analysis[a]

	$TBA_{0.24}H_{0.76}Ca_2Nb_3O_{10}$	Na-TSM
metal NP	diameter (nm) (n)	diameter (nm) (n)
$IrO_x\cdot nH_2O$	0.9 ± 0.2 (151)	1.3 ± 0.5 (53)
$Co(OH)_2$	1.2 ± 0.5 (304)	2.1 ± 0.5 (154)
$Ni(OH)_2$	1.3 ± 0.4 (153)	6 ± 3 (201)
CuO	2.0 ± 0.6 (320)	6 ± 5 (66)
Ag_2O	7 ± 5 (216)	5 ± 2 (219)

[a]The number in parentheses represents the number of measurements used to determine one standard deviation of the mean.

DOI: 10.1021/jacs.5b11230
J. Am. Chem. Soc. 2015, 137, 16216−16224

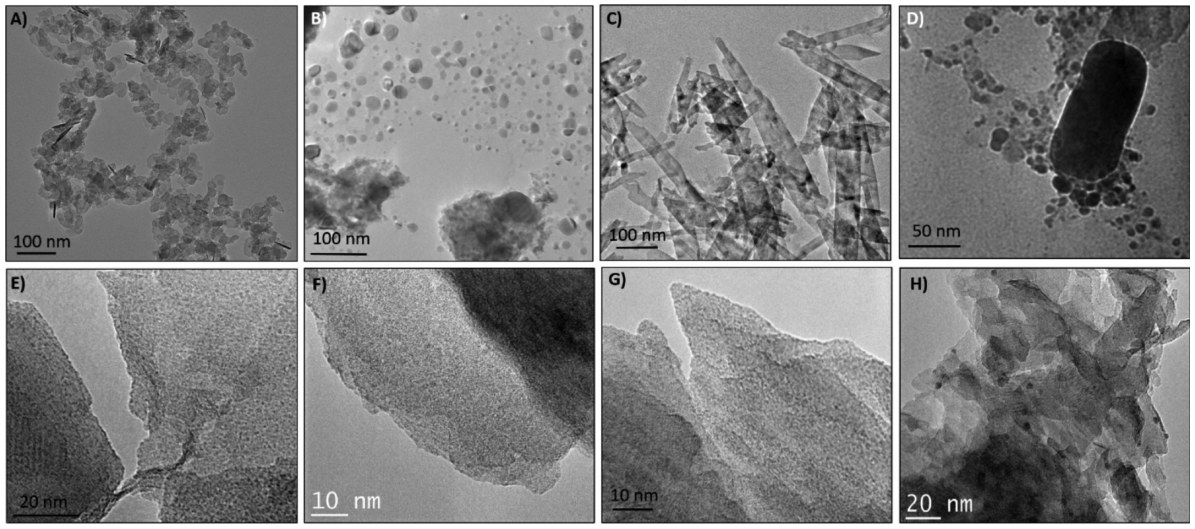

Figure 2. TEM images from "reverse" ripening experiments in which preformed particles were mixed with suspensions of $TBA_{0.24}H_{0.76}Ca_2Nb_3O_{10}$ nanosheets. Panels A–D show preformed particles of $Co(OH)_2$, $Ni(OH)_2$, CuO and Ag_2O, respectively. E–H show the nanoparticles derived from the same elements, respectively, after deposition onto the nanosheets.

Scheme 1. General Born–Haber Cycle for Metal Oxide/Hydroxide Nanoparticle Deposition onto Oxide Supports during ITC Experiments

$$(1)\ HCl_{(aq)} + TBA^+OH^-_{(aq)} \rightarrow TBA^+Cl^-_{(aq)} + H_2O_{(l)} \qquad \Delta H_1$$

$$(2)\ MX_{n(aq)} + nTBA^+OH^-_{(aq)} \rightarrow M(O/OH)_{n(s)} + nTBA^+X^-_{(aq)} \qquad \Delta H_2$$

$$(3)\ M(O/OH)_{n(s)} + TBA^+/\ sheets^-_{(s)} \rightarrow M(O/OH)_n/TBA^+/sheets^-_{(s)} \qquad \Delta H_3$$

$$(4)\ MX_{n(aq)} + (1+n)TBA^+OH^-_{(aq)} + HCl_{(aq)} + TBA^+/\ sheets^-_{(s)} \rightarrow M(O/OH)_n/TBA^+/sheets^-_{(s)} + TBA^+Cl^-_{(aq)} + nTBA^+X^-_{(aq)} + H_2O_{(l)} \qquad \Delta H_4$$

there is a spatially uniform distribution of nanoparticles on the niobate support. The average diameter of the Ag_2O particles (7 nm) is much larger than the other deposited nanoparticles (1–2 nm).

For comparison purposes, the same nanoparticles were deposited onto the layered silicate Na-TSM. Na-TSM contains tetrahedral-octahedral-tetrahedral (T-O-T) silicate layers separated by Na^+ ions (Figure S4). Each tetrahedral layer is capped by oxygen atoms shared by two T atoms, and therefore there are no free Si–OH groups on the basal plane surface. The saturation loading of nanoparticles and their distribution onto Na-TSM was in stark contrast to nanoparticles deposited onto $KCa_2Nb_3O_{10}$, as shown in the bottom row of images in Figure 1. There was a broader size distribution of nanoparticles, as well as areas of the support with no nanoparticles present, and there were also large particles in the suspension, as seen in the TEM, that were not bound to the support in the case of both CuO and Ag_2O.

In our earlier study, micron-sized $Rh(OH)_3$ particles were found to break up and deposit as <1 nm diameter particles on nanosheets of $TBA_{0.24}H_{0.76}Ca_2Nb_3O_{10}$.[26] This "reverse" ripening effect was attributed to the thermodynamically favorable interaction between $Rh(OH)_3$ and the oxide support, which overcomes the surface energy penalty of forming smaller particles. "Reverse" ripening experiments were performed on Co, Ni, Cu, and Ag oxide/hydroxide particles by hydrolyzing the metal halide precursors in TBA^+OH^- for 18 h before their addition to a suspension of $TBA_{0.24}H_{0.76}Ca_2Nb_3O_{10}$ nanosheets in 25 mmol L^{-1} TBA^+OH^-.

In all cases, the deposited nanoparticles were smaller after addition of the nanosheet suspension, and in a few cases, the shape of the nanoparticles changed dramatically. For example, CuO particles formed in the absence of nanosheets were rods with an outer diameter of (19 ± 13) nm (n = 95), $Co(OH)_2$ particles were both thin platelets with an average lateral dimension of (22 ± 11) nm (n = 193) and rods, and $Ni(OH)_2$ particles were a mixture of spherical particles, platelets and wires (not all shapes are pictured in Figure 2b). Upon addition of the preformed metal oxide/hydroxide particles to colloidal $TBA_{0.24}H_{0.76}Ca_2Nb_3O_{10}$, all the metal oxides/hydroxides deposited as much smaller nanoparticles and no rod-shaped particles were found. Not all of the preformed $Co(OH)_2$ and Ag_2O particles deposited on the nanosheets, and $Co(OH)_2$ particles deposited with a broad size distribution on different areas of the nanosheets. Figure 2 shows TEM images of the preformed nanoparticles (top) and their deposition onto $TBA_{0.24}H_{0.76}Ca_2Nb_3O_{10}$ nanosheets (bottom).

ITC Measurements of Interfacial Bonding Energies. The interaction heats between metal oxide/hydroxide nanoparticles and oxide supports were measured by using ITC titrations as previously described.[26] The deposition of the nanoparticles onto an oxide support involves several chemical steps, and therefore, the enthalpy change that corresponds to the nanoparticle–support interaction must be obtained by difference from the overall heat of reaction.

Scheme 1 shows a generic Born–Haber cycle for the deposition of a metal oxide/hydroxide ($M(O/OH)_{(s)}$) from a metal halide precursor ($MX_{(aq)}$). The overall enthalpy change

DOI: 10.1021/jacs.5b11230
J. Am. Chem. Soc. 2015, 137, 16216–16224

of the reaction (ΔH_4) is the sum of the enthalpies of bonding (ΔH_3), hydrolysis (ΔH_2), and neutralization (ΔH_1). This Born−Haber cycle was used for cobalt, nickel, copper and silver deposition. The enthalpy of neutralization (ΔH_1 = (−58 ± 2) kJ mol^{-1}) was included only in cases when hydrolysis of the metal salt precursor generated acid. The deposition of iridium oxide represents a special case, since we have recently found that colloidal solutions of ligand-free $IrO_x{\cdot}nH_2O$ nanoparticles prepared by alkaline hydrolysis of $[IrCl_6]^{2-}$ solutions contain strongly adsorbed hydroxyiridate ions $[Ir(OH)_5(H_2O)]^{2-}$ and $[Ir(OH)_6]^{2-}$.[32] ITC experiments were performed to measure the heats of adsorption of each individual component. First, the $IrO_x{\cdot}nH_2O$ colloidal solution was purified as previously reported to remove the monomeric anions from the surface of the nanoparticles.[32] Interestingly, there was no measurable heat of interaction between these purified particles and $TBA_{0.24}H_{0.76}Ca_2Nb_3O_{10}$ nanosheets. Next, the heat of interaction between the monomeric anions and nanosheets was measured and found to be −83 ± 17 kJ mol^{-1}. From these data, it could be concluded that only the monomeric anions are interacting with the support when $IrO_x{\cdot}nH_2O$ nanoparticles are deposited onto the nanosheets. Therefore, we use the interaction heat of the monomeric anions in plotting the periodic trends below (Figure 3). It should be noted that

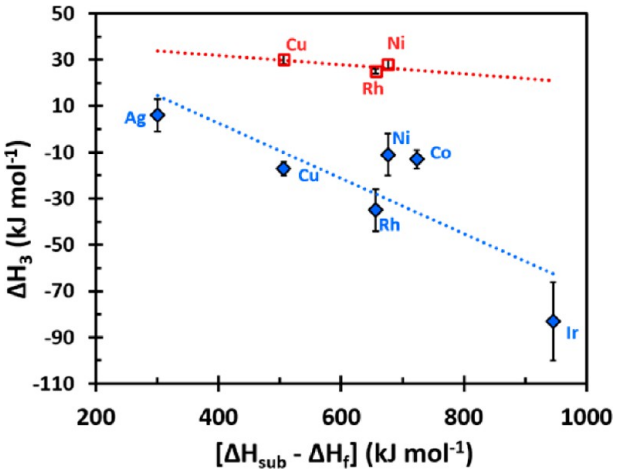

Figure 3. Thermochemical data for heats of interaction between metal oxide/hydroxide nanoparticles (or monomeric anions in the case of Ir) and supports for $TBA_{0.24}H_{0.76}Ca_2Nb_3O_{10}$ nanosheets (blue diamonds) and high surface area silica (red squares). The SiO_2 nanoparticle support had an average particle diameter of (17 ± 6) nm (n = 101) and a surface area of (408 ± 8) m^2 g^{-1}. Enthalpy changes are plotted per mole of transition metal M. The x-axis represents M−O bond strength as the difference between the heat of sublimation of the bulk metal and the heat of formation of its most stable oxide.

alkaline solutions of the monomer in equilibrium with air contain both Ir^{III} and Ir^{IV} forms of the monomer ($[Ir(OH)_5(H_2O)]^{2-}$ and $[Ir(OH)_6]^{2-}$, respectively), but EPR experiments show that the predominant form is Ir^{III},[32] and therefore we refer to the equilibrium mixture of anions simply as $[Ir(OH)_5(H_2O)]^{2-}$.

Figure 3 shows the molar enthalpy of adsorption of the metal nanoparticles (or monomer in the case of Ir^{III}) to $TBA_{0.24}H_{0.76}Ca_2Nb_3O_{10}$ nanosheets, plotted against [ΔH_{sub} − ΔH_f], the difference between the sublimation enthalpy of the bulk metal and the heat of formation of the most stable metal oxide (experimental values of ΔH_{sub} and ΔH_f used for each metal are provided in Table S2). This quantity represents the heat of forming the metal oxide from metal atoms and thus follows the trend in M−O bond energy. These enthalpy changes are plotted as kJ per mole of metal atoms. The ΔH_3 values span a broad range, from quite exothermic to mildly endothermic. The strongest bonding to the niobate sheets is $[Ir(OH)_5(H_2O)]^{2-}$ with an interaction heat of (−83 ± 17) kJ mol^{-1}, while the weakest is with Ag_2O at (6 ± 7) kJ mol^{-1}. This endothermic heat of interaction can be measured since the enthalpy of the overall reaction is favorable; that is, reactions 1 and 2 drive the adsorption of nanoparticles to the support. The general trend is toward weaker interfacial bonding as the strength of the M−O bond in the bulk oxide decreases, as observed in earlier calorimetric studies of metal clusters binding to oxide supports,[5] although this is the first demonstration of this correlation for binding from a liquid-phase metal precursor solution. While the same trend is followed for metals on the silica support, in that case, the interaction energies are endothermic and there is less of a difference between elements with stronger and weaker M−O bonding.

It is apparent from the comparison of Table 1 and Figures 2 and 3 that well-dispersed and smaller nanoparticles are grown on the niobate support as the heat of interaction becomes more exothermic. Upon deposition, $Rh(OH)_3$ nanoparticles on $TBA_{0.24}H_{0.76}Ca_2Nb_3O_{10}$ have an average diameter of less than 1 nm and a heat of interaction of (−35 ± 9) kJ mol^{-1}.[26] In contrast Ag_2O has a slightly endothermic interaction heat (6 ± 7) kJ mol^{-1} and deposits at room temperature as unevenly distributed particles with an average size diameter of (7 ± 5) nm. The broad distribution of particle sizes for the metal oxides studied on Na-TSM (Table 1) correlates with the endothermic interaction energy with the high surface area silica support. The resistance of supported nanoparticles to sintering (see Supporting Information) follows a similar trend in which the thermodynamic driving force for particle growth is reduced by a strong bonding interaction of the nanoparticle with the support. Therefore, hydroxyiridate-capped $IrO_x{\cdot}nH_2O$ nanoparticles deposited on a niobium support are remarkably resistant to sintering at temperatures up to 1000 °C (Figure 4).

Computational Modeling of Particle-Support Interactions. Campbell and co-workers have shown that metals that bond more strongly to oxygen also interact more exothermically with oxide supports.[5] In their experiments, like those described here, the composition of the support has a clear effect on the strength of this interaction.[5] "Strong" supports such as CeO_2 and Fe_3O_4 are differentiated from "weak" supports such as MgO by their more exothermic bonding to noble metal nanoparticles.[4,5] To better understand the nature of the interfacial interaction, the first set of DFT electronic structure calculations done in this work used a range of metals (Au, Ag, Cu, Pt, Pd, Ni, Ir, Rh, and Co) and models for representative oxide supports ($HCa_2Nb_3O_{10}$ and SiO_2). Because the extent of nanoparticle reduction in the experimental particle growth studies is unknown, and since previous experiments show similar trends for growth of $Rh(OH)_3$ nanoparticles when heated in vacuum and reducing atmospheres, we initially used fully reduced metal atoms and clusters to simplify the modeling. The calculations were then extended to metal atoms and clusters in higher oxidation states, which qualitatively show the same trends in bonding strength (see below).

The calcium niobate nanosheets were modeled in their proton-exchanged form ($HCa_2Nb_3O_{10}$) by first optimizing the bulk structure, beginning with the experimentally characterized

DOI: 10.1021/jacs.5b11230
J. Am. Chem. Soc. 2015, 137, 16216−16224

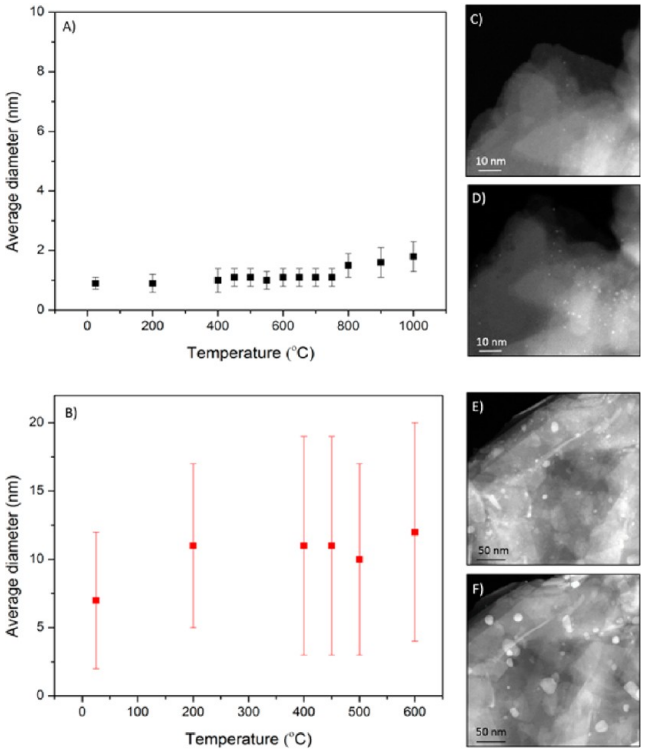

Figure 4. Plots of the average particle diameter of (A) hydroxyiridate-capped $IrO_x \cdot nH_2O$ and (B) Ag_2O deposited on $TBA_{0.24}H_{0.76}Ca_2Nb_3O_{10}$ nanosheets, after restacking with KOH. The uncertainty in each measurement is reported as one standard deviation of the mean for n measurements (Supporting Information, Table S3). HAADF STEM images of hydroxyiridate-capped $IrO_x \cdot nH_2O$ supported on $KCa_2Nb_3O_{10}$ at (C) 25 °C and (D) 700 °C. (E) and (F) are HAADF STEM images of Ag_2O on $KCa_2Nb_3O_{10}$ at 25 and 700 °C, respectively.

*P*4/*mbm* crystal structure refined by Chen et al.[29] The DFT-optimized bulk lattice constants were $a = b = 0.534$ nm and $c = 1.464$ nm, in reasonable agreement with the experimental values of $a = b = 0.545$ nm and $c = 1.441$ nm. From the optimized computed structure, the surface of the layered oxide was cleaved in the [001] direction, which is the layering axis of the crystal. H_2O molecules that occupy the interlayer galleries in the bulk structure were not included in the computational model. The resulting surface structure of the $HCa_2Nb_3O_{10}$ support is shown in Figure S7.

The SiO_2 support was modeled using a reconstructed, partially hydroxylated β-cristobalite $SiO_2(001)$ surface structure reported by Rozanska et al., which is predicted to be stable under the conditions employed in this study and is commonly used to model amorphous silica supports.[41]

Binding energies for both single metal atoms and four-atom tetrahedral clusters (denoted M_4) were calculated to model metal-oxide support interaction strengths. Binding energies were calculated relative to the clean oxide surface plus a gas phase metal atom (or cluster): $E_{bind} = E_{metal/support} - E_{support\text{-}[clean]} - E_{metal\text{-}[g]}$, where $E_{metal\text{-}[g]}$ is the energy of the gas phase metal atom (or cluster), $E_{support\text{-}[clean]}$ is the energy of the clean support surface, and $E_{metal/support}$ is the energy of the metal-adsorbed surface. Negative values indicate exothermic binding. It is important to note that these calculations do not include solvation terms that are important in the ITC experiments, so we expect them to reproduce periodic trends but not to give the same energy changes as those measured experimentally.

For single atoms, structural optimization calculations were initiated from three possible surface binding sites on the $HCa_2Nb_3O_{10}$ surface: (1) the equatorial oxygen, (2) the axial oxygen, or (3) the interstitial space between NbO_6 polyhedra (Figure S7A). The optimized structure of Ir and Ag atoms are shown in Figure 5A and 5B, respectively, and demonstrate that

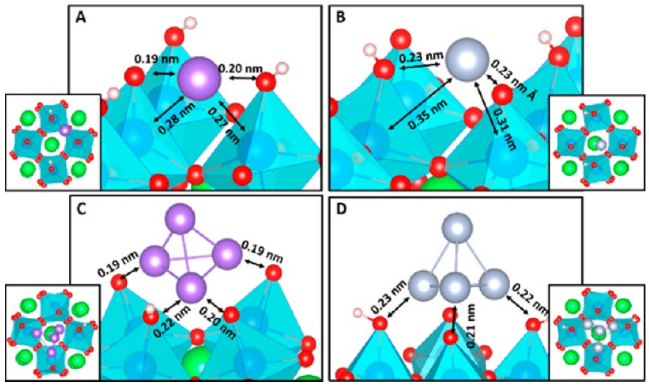

Figure 5. Optimized adsorption geometries and internuclear distances on $HCa_2Nb_3O_{10}$ for single atoms of (A) Ir and (B) Ag and for M_4 clusters of (C) Ir and (D) Ag.

the equatorial oxygen site is preferred for Ir, which interacts strongly, whereas the interstitial site is preferred for Ag, which interacts more weakly. In both cases, there is a resulting close contact between the adsorbed metal and niobium atoms in the support. For Ir and Ag, the optimized metal−niobium internuclear distances are 0.27 and 0.31 nm, respectively. This suggests that metal−metal bonding between the adsorbed metal and the underlying niobium atom is indeed possible. The optimized structure of all the metal atoms studied on $HCa_2Nb_3O_{10}$ are shown in Figure S8, where metal−metal bond distances (Table S4) between 0.18 and 0.23 nm were calculated in all cases. The optimized single atom metal adsorption site for SiO_2 binding is the same for all metals and is represented in Figure S9.

The optimized M_4 adsorption structures for Ir and Ag on $HCa_2Nb_3O_{10}$ are provided in Figure 5C and 5D, respectively. Both of these metallic clusters prefer the interstitial bonding site with a 3-atom basal plane in contact with surface oxygen atoms, where Ag_4 sits higher above the oxide surface compared to Ir_4. The optimized M_4 adsorption structures for all the metals, shown in Figure S10, demonstrate that all metals (except Au) prefer the interstitial site with the 3-atom basal plane in contact with the surface. The bond distances are shown in Table S5.

In Figure 6A,B, the resulting binding energies are plotted against $[\Delta H_{sub} - \Delta H_f]$ for each metal. A linear correlation between the oxide formation energy and the metal−support binding strength emerges from the calculations. The niobate and silicate supports are strong and weak, respectively, as also shown in the experimental data in Figure 3.

This type of correlation was first proposed and experimentally demonstrated by Campbell and Sellers[5] and can serve as a useful computational screening tool for selecting candidates for supported catalytic metals with specific interaction strengths. The plots in Figure 6 demonstrate that platinum-group metals bind strongly to the niobate support, whereas late

DOI: 10.1021/jacs.5b11230
J. Am. Chem. Soc. 2015, 137, 16216−16224

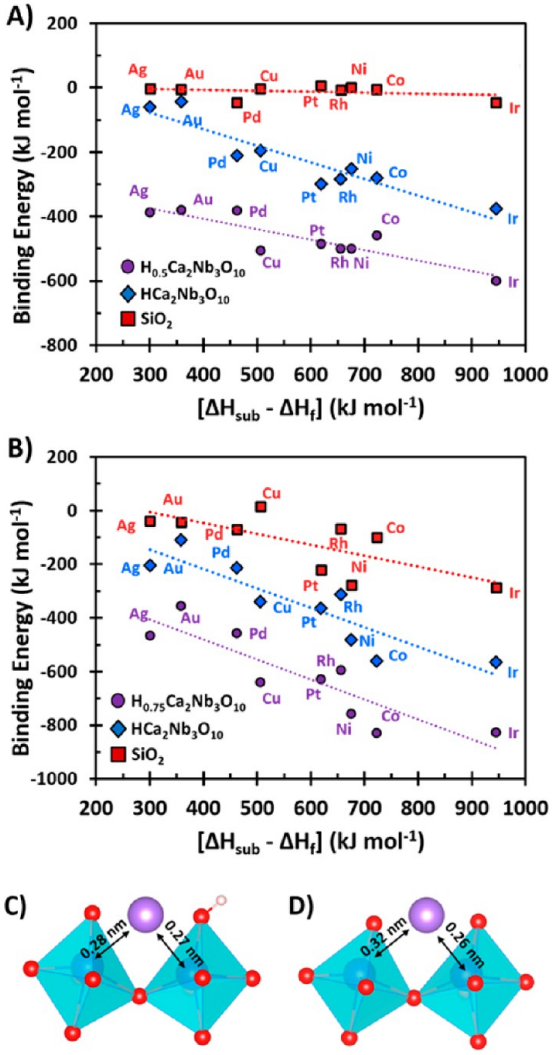

Figure 6. Binding energies for (A) single metal atoms and (B) M_4 metal clusters on niobium oxide and silica surfaces plotted against the formation enthalpy of the corresponding metal's most stable oxide calculated relative to a single gas phase metal atom, $[\Delta H_{sub} - \Delta H_f]$. Structural interfaces of iridium adsorbed to (C) stoichiometric and (D) nonstoichiometric niobium oxide surfaces.

transition metals interact weakly with the silica support. The resulting periodic trend in interaction strength across late transition metal atoms and clusters is in agreement with the experimental trend in adsorption strengths of metal oxides (ΔH_3) determined by ITC and shown in Figure 3. The DFT calculations are also consistent with the experimental observation that the composition of the support strongly affects the interfacial bonding enthalpy. All metal nanoparticles investigated interact weakly with the SiO_2 support, as shown experimentally in Figure 3 and computationally in Figure 6.

The effect of the oxidation state of the metal atom was then investigated for comparison with the experimentally measured heats of interaction determined by ITC. The binding energies of all metals were calculated on an $H_{0.5}Ca_2Nb_3O_{10}$ surface model, which changed the formal oxidation state of the metal from M^0 to M^{1+}. This yields an oxidation state equivalent to adsorbing a metal atom with an attached −OH group (and desorbing H_2O in the adsorption process). The data in Figure 6A show stronger adsorption to the $H_{0.5}Ca_2Nb_3O_{10}$ surface than to the stoichiometric surface, and the same qualitative trend in bonding strength is obtained regardless of the oxidation state of the metal. Figure 6C–D compares the structural interface models of iridium calculated in different oxidation states. The Ir–Nb bond distance is decreased over the $H_{0.5}Ca_2Nb_3O_{10}$ surface, reflecting stronger binding induced by the Ir–Nb interaction. The good correlation between theory and experiment suggests that the periodic trends in nanoparticle/support interactions are insensitive to the metal oxidation state, as observed experimentally in the $Rh/Rh(OH)_3$ case.[26] This suggests that DFT modeling can be used to investigate a broader range of metals than might be experimentally accessible for ITC thermodynamic analysis.

Analysis of metal–support electronic structures provides insight into the nature of the metal-oxide support bonding. The difference in bonding character between Ir and Ag on the niobium oxide is demonstrated by the density of states (DOS) analysis shown in Figure 7. In Figure 7A, there is clear mixing of

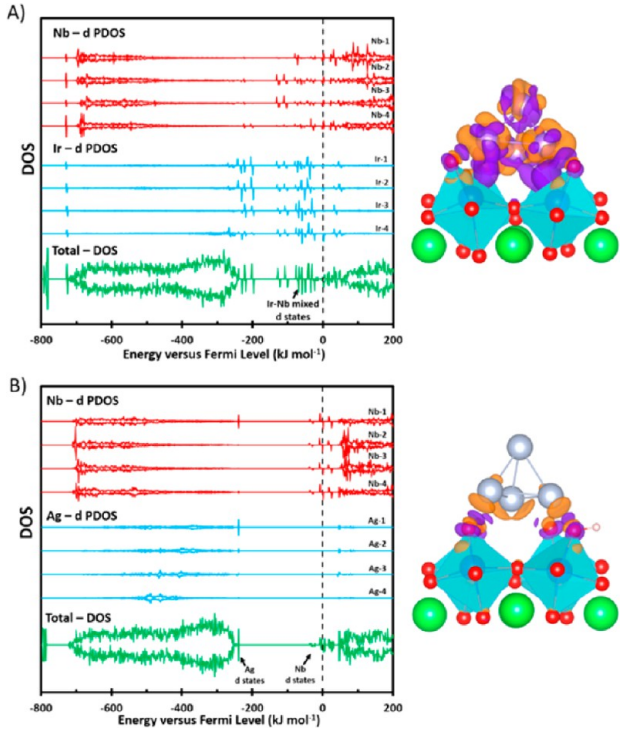

Figure 7. Total and partial density of states plotted relative to the Fermi level for $HCa_2Nb_3O_{10}$ supported (A) Ir and (B) Ag 4-atom clusters. The total DOS is shown in green, the PDOS projected on the d-states of the Nb surface atom adjacent to the adsorbed metal atom is shown in red, and PDOS projected on the d-states of the adsorbed metal atom is shown in blue. Spin up and spin down states are plotted on the positive and negative axes, respectively. The Fermi level is denoted by the vertical dotted line. Charge density difference isosurfaces are shown on the right, where the purple regions reflect negative charge accumulation and the orange regions reflect charge depletion. The accumulation and depletion isosurfaces are shown at values of $\pm 0.4\ e\ nm^{-1}$.

Ir and Nb d-states, indicative of electron transfer from Ir atoms to the nearest adjacent niobium atoms in the support. This suggests some degree of metal–metal bonding and is further confirmed by the Bader charge differences (calculated as the Bader charge of the surface-bound metal atom relative to the valence of the gas phase metal atom) reported in Table S6. A pronounced negative charge depletion on the surface-bound Ir

DOI: 10.1021/jacs.5b11230
J. Am. Chem. Soc. 2015, 137, 16216–16224

atom is observed. The isostructural plots in Figure 7 show the charge density difference calculated between the full metal−support system and the clean-support/metal-atom components, revealing how charge is transferred between the cluster and the support. For the iridium cluster, there is significant valence electron density between Ir and Nb at the interface demonstrated by the purple isosurface, which again suggest a strong Ir−Nb bonding interaction. Conversely, no mixing of d-states between Ag and niobium is seen in the DOS plots in Figure 7B, resulting in a high energy gap state relative to the d-band and weak Ag binding. Correspondingly, there is no valence electron density accumulation between the cluster and support in the Ag system seen in the charge density difference. This conclusion is also consistent for the bonding between the niobium support and single metal atoms, as shown in Figures S11 and S12, demonstrating that the results are not dependent on the chosen cluster model.

The Bader charge analysis for $HCa_2Nb_3O_{10}$ in Table S6 demonstrates that for all metals tested there is significant *negative charge transfer* from the transition metal atom to the niobate support, whereas there is little charge transfer to or from the transition metal to SiO_2. In fact, for Ir and Ni on SiO_2, there is actually a small amount of charge transfer *from* the support to the adsorbed metal; this is also reflected in the charge density difference plot for Ir-SiO_2 shown in Figure S13.

The role of d-orbital mixing in stabilizing bimetallic transition metal alloys and interfaces has a long history in the experimental and theoretical literature. Brewer proposed in 1967 that d-acid/base interactions between early and late transition metals, respectively, could account for the anomalous stability of alloys such as $ZrPt_3$.[42] Later electronic structure calculations by Wang and Carter, however, showed that in these alloys charge transfer occurred in the opposite direction, from the early to the late transition metal.[43] Strong evidence for electron transfer in the Brewer sense (from the more to the less electronegative metal) has been found for ultrathin films of late transition metals such as Pd, Ni, and Cu on earlier transition metal (Mo, W, Ru) surfaces.[44−47] In these studies, Goodman concluded that the electronegativity of the surface atoms was lower than those in the bulk metal.[45] The present results suggests that the Brewer d-acid/base interaction is quite relevant to the interaction of transition metal and metal oxide nanoparticles with "strong" supports, which have empty or partially filled d-orbitals. A key factor appears to be the coincidence of d-orbital energies in the relevant oxidation states of the two metals, as shown for Ir^0 and Nb^{5+} in Figure 7A. It is interesting to note that Ag binds weakly to the niobate support because the d-orbitals of Ag are significantly lower in energy than those of Nb^{5+}. As demonstrated in Figures 3 and 6, metals that form stronger M−O bonds are also observed to bind stronger to the oxide support. Our electronic structure analysis, however, suggests that electron donation from the adsorbed metal atom occurs mainly to the Nb on the layered niobate structures, suggesting that the supported metal atoms oxidation tendencies can be predictive of strong support interactions independent from the destination of charge transferred upon adsorption. This suggests the possibility of tuning the strength of the metal−support interactions for late transition metals through appropriate choice of d-electron accepting oxide supports. Experiments along these lines are currently underway

CONCLUSIONS

Metal oxide and hydroxide nanoparticles (M = Co, Ni, Cu, Ag) and monomeric $[Ir(OH)_5(H_2O)]^{2-}$ anions were deposited onto niobium oxide and silicon oxide supports by alkaline hydrolysis of water-soluble metal salts. ITC and TEM data show a strong correlation between interfacial bonding strength and the inhibition of thermal sintering of the supported nanoparticles. These results are consistent with our earlier observations of $Rh(OH)_3$ nanoparticles on early transition metal oxide and main group oxide supports.[26] Nanoparticles that bond exothermically to the oxide support, such as hydroxyiridate-capped $IrO_x{\cdot}nH_2O$ on $KCa_2Nb_3O_{10}$, deposit as <1 nm particles and resist sintering even up to temperatures of 1000 °C. In contrast, nanoparticles that interact endothermically with silica supports have a broad original size distribution and appear to migrate and coalesce rapidly at lower temperatures.

ITC data show that $Ni(OH)_2$, CuO and $Rh(OH)_3$ all interact endothermically with SiO_2 and exothermically with $TBA_{0.24}H_{0.76}Ca_2Nb_3O_{10}$ nanosheets. This trend is supported by DFT calculations, which also provide insight into the nature of the metal−support interaction. The strong interaction between late transition metal/metal oxide nanoparticles and the early transition metal oxide support $HCa_2Nb_3O_{10}$ can be attributed to the formation of mixed d-states and charge transfer from the supported metal atoms to the niobium atoms in the oxide support. These interactions are absent in weakly binding metals and a silicon oxide support. A strong correlation between the experimental measurements and theoretical calculations emerged in this work to confirm that the qualitative trends in metal bonding interaction are independent of the formal oxidation state of the supported metal. Together, these combined experimental and computational studies reveal the important role of d-orbital interactions in controlling the metal−support interaction, and underscore the importance of understanding how the support composition impacts nanoparticle bonding strength and stability.

ASSOCIATED CONTENT

Supporting Information

The Supporting Information is available free of charge on the ACS Publications website at DOI: 10.1021/jacs.5b11230.

Details of obtaining thermochemical data from ITC experiments, XRD of bulk nanoparticles and nanoparticle/support composites, TEM and UV−vis of hydroxyiridate-capped $IrO_x{\cdot}nH_2O$ particles, sintering studies of supported metal oxide nanoparticles, surface models used for DFT binding energy calculations, optimized single atom and metal cluster adsorption geometries, charge density difference plots, list of nanoparticles and metal precursors, and heats of formation of oxides and sublimation of metals (17 pp). (PDF)

AUTHOR INFORMATION

Corresponding Authors

*mjanik@engr.psu.edu

*tem5@psu.edu

Notes

The authors declare no competing financial interest.

DOI: 10.1021/jacs.5b11230
J. Am. Chem. Soc. 2015, 137, 16216−16224

■ ACKNOWLEDGMENTS

We thank Nicholas McCool for assistance with obtaining ambient temperature TEM images and helpful discussions, and Nicholas Sturgis for helpful ITC discussions. This work was supported by the National Science Foundation under grant DMR-1306938. MES and NMVB acknowledge National Science Foundation Graduate Fellowship grant DGE-1255832. TPS and MJJ acknowledge support from National Science Foundation grant CBET-1032979. RMR acknowledges funding from the Department of Energy, Office of Basic Energy Sciences, Chemical Sciences, Geosciences and Biosciences Division, Catalysis Sciences Program, under grant number DE-FG02-12ER16364. Additionally, RMR acknowledges funding from the Pennsylvania State University College of Engineering Instrumentation Grant Program for the purchase of a TA Instruments NanoITC.[48]

■ REFERENCES

(1) Goodman, D. W. *Chem. Rev.* **1995**, *95*, 523−536.
(2) Haruta, M. *Catal. Today* **1997**, *36*, 153−166.
(3) Shekhar, M.; Wang, J.; Lee, W.-S.; Williams, W. D.; Kim, S. M.; Stach, E. A.; Miller, J. T.; Delgass, W. N.; Ribeiro, F. H. *J. Am. Chem. Soc.* **2012**, *134*, 4700−4708.
(4) Campbell, C. T. *Acc. Chem. Res.* **2013**, *46*, 1712−1719.
(5) Campbell, C. T.; Sellers, J. R. V. *Faraday Discuss.* **2013**, *162*, 9−30.
(6) Cargnello, M.; Doan-Nguyen, V. V. T.; Gordon, T. R.; Diaz, R. E.; Stach, E. A.; Gorte, R. J.; Fornasiero, P.; Murray, C. B. *Science* **2013**, *341*, 771−773.
(7) Valden, M.; Lai, X.; Goodman, D. W. *Science* **1998**, *281*, 1647−1650.
(8) Vayssilov, G. N.; Lykhach, Y.; Migani, A.; Staudt, T.; Petrova, G. P.; Tsud, N.; Skála, T.; Bruix, A.; Illas, F.; Prince, K. C.; Matolín, V. r.; Neyman, K. M.; Libuda, J. *Nat. Mater.* **2011**, *10*, 310−315.
(9) Mostafa, S.; Behafarid, F.; Croy, J. R.; Ono, L. K.; Li, L.; Yang, J. C.; Frenkel, A. I.; Cuenya, B. R. *J. Am. Chem. Soc.* **2010**, *132*, 15714−15719.
(10) Haruta, M. *CATTECH* **2002**, *6*, 102−115.
(11) Bonanni, S.; Aït-Mansour, K.; Harbich, W.; Brune, H. *J. Am. Chem. Soc.* **2012**, *134*, 3445−3450.
(12) Hu, Z.; Nakamura, H.; Kunimori, K.; Asano, H.; Uchijima, T. *J. Catal.* **1988**, *112*, 478−488.
(13) Tauster, S. J. *Acc. Chem. Res.* **1987**, *20*, 389−394.
(14) Tauster, S. J.; Fung, S. C.; Baker, R. T. K.; Horsley, J. A. *Science* **1981**, *211*, 1121−1125.
(15) Wang, Y.-G.; Yoon, Y.; Glezakou, V.-A.; Li, J.; Rousseau, R. *J. Am. Chem. Soc.* **2013**, *135*, 10673−10683.
(16) Meyer, R.; Ge, Q.; Lockemeyer, J.; Yeates, R.; Lemanski, M.; Reinalda, D.; Neurock, M. *Surf. Sci.* **2007**, *601*, 134−145.
(17) Addou, R.; Senftle, T. P.; O'Connor, N.; Janik, M. J.; van Duin, A. C. T.; Batzill, M. *ACS Nano* **2014**, *8*, 6321−6333.
(18) Negreiros, F. R.; Fabris, S. *J. Phys. Chem. C* **2014**, *118*, 21014−21020.
(19) Vilhelmsen, L. B.; Hammer, B. *Phys. Rev. Lett.* **2012**, *108*, 126101-1−126101-5.
(20) Bruix, A.; Lykhach, Y.; Matolínová, I.; Neitzel, A.; Skála, T.; Tsud, N.; Vorokhta, M.; Stetsovych, V.; Ševčíková, K.; Myslivecek, J.; Fiala, R.; Václavů, M.; Prince, K. C.; Bruyère, S.; Potin, V.; Illas, F.; Matolín, V.; Libuda, J.; Neyman, K. M. *Angew. Chem., Int. Ed.* **2014**, *53*, 10525−10530.
(21) Hansen, T. W.; DeLaRiva, A. T.; Challa, S. R.; Datye, A. K. *Acc. Chem. Res.* **2013**, *46*, 1720−1730.
(22) Fu, Q.; Yang, F.; Bao, X. *Acc. Chem. Res.* **2013**, *46*, 1692−1701.
(23) Hansen, P. L.; Wagner, J. B.; Helveg, S.; Rostrup-Nielsen, J. R.; Clausen, B. S.; Topsøe, H. *Science* **2002**, *295*, 2053−2055.
(24) Campbell, C. T.; Parker, S. C.; Starr, D. E. *Science* **2002**, *298*, 811−814.
(25) Prieto, G.; Zečević, J.; Friedrich, H.; de Jong, K. P.; de Jongh, P. E. *Nat. Mater.* **2013**, *12*, 34−39.
(26) Strayer, M. E.; Binz, J. M.; Tanase, M.; Kamali Shahri, S. M.; Sharma, R.; Rioux, R. M.; Mallouk, T. E. *J. Am. Chem. Soc.* **2014**, *136*, 5687−5696.
(27) Stuckless, J. T.; Frei, N. A.; Campbell, C. T. *Rev. Sci. Instrum.* **1998**, *69*, 2427−2438.
(28) Dion, M.; Ganne, M.; Tournoux, M. *Mater. Res. Bull.* **1981**, *16*, 1429−1435.
(29) Chen, Y.; Zhao, X.; Ma, H.; Ma, S.; Huang, G.; Makita, Y.; Bai, X.; Yang, X. *J. Solid State Chem.* **2008**, *181*, 1684−1694.
(30) Hata, H.; Kobayashi, Y.; Bojan, V.; Youngblood, W. J.; Mallouk, T. E. *Nano Lett.* **2008**, *8*, 794−799.
(31) Ma, R.; Kobayashi, Y.; Youngblood, W. J.; Mallouk, T. E. *J. Mater. Chem.* **2008**, *18*, 5982−5985.
(32) Zhao, Y.; Vargas-Barbosa, N. M.; Strayer, M. E.; McCool, N.; Pandelia, M.-E.; Saunders, T.; Swierk, J.; Callejas, J.; Jensen, L.; Mallouk, T. E. *J. Am. Chem. Soc.* **2015**, *137*, 8749−8757.
(33) Kresse, G.; Furthmuller, J. *Comput. Mater. Sci.* **1996**, *6*, 15−50.
(34) Kresse, G.; Furthmuller, J. *Phys. Rev. B: Condens. Matter Mater. Phys.* **1996**, *54*, 11169−11186.
(35) Perdew, J. P.; Chevary, J. A.; Vosko, S. H.; Jackson, K. A.; Pederson, M. R.; Singh, D. J.; Fiolhais, C. *Phys. Rev. B: Condens. Matter Mater. Phys.* **1992**, *46*, 6671−6687.
(36) Kresse, G.; Joubert, D. *Phys. Rev. B: Condens. Matter Mater. Phys.* **1999**, *59*, 1758−1775.
(37) Monkhorst, H. J.; Pack, J. D. *Phys. Rev. B* **1976**, *13*, 5188−5192.
(38) Bader, R. F. W. *Acc. Chem. Res.* **1985**, *18*, 9−15.
(39) Henkelman, G.; Arnaldsson, A.; Jonsson, H. *Comput. Mater. Sci.* **2006**, *36*, 354−360.
(40) Zhao, Y.; Hernandez-Pagan, E. A.; Vargas-Barbosa, N. M.; Dysart, J. L.; Mallouk, T. E. *J. Phys. Chem. Lett.* **2011**, *2*, 402−406.
(41) Rozanska, X.; Delbecq, F.; Sautet, P. *Phys. Chem. Chem. Phys.* **2010**, *12*, 14930−14940.
(42) Brewer, L. *Acta Metall.* **1967**, *15*, 553−556.
(43) Wang, H.; Carter, E. A. *J. Am. Chem. Soc.* **1993**, *115*, 2357−2362.
(44) Campbell, R. A.; Rodriguez, J.; Goodman, D. W. *Surf. Sci.* **1990**, *240*, 71−80.
(45) Rodriguez, J. A.; Campbell, R. A.; Goodman, D. W. *J. Phys. Chem.* **1991**, *95*, 5716−5719.
(46) Rodriguez, J. A.; Goodman, D. W. *J. Phys. Chem.* **1991**, *95*, 4196−4206.
(47) Heitzinger, J. M.; Gebhard, S. C.; Koel, B. E. *Surf. Sci.* **1992**, *275*, 209−222.
(48) Certain commercial equipment, instruments, or materials (or suppliers, or software, ...) are identified in this paper to foster understanding. Such identification does not imply recommendation or endorsement by the National Institute of Standards and Technology, nor does it imply that the materials or equipment identified are necessarily the best available for the purpose.

DOI: 10.1021/jacs.5b11230
J. Am. Chem. Soc. 2015, 137, 16216−16224